First-order finite-Larmor-radius fluid modeling of tearing and relaxation in a plasma pinch

J. R. King, C. R. Sovinec, and V. V. Mirnov

Additional information on Phys. Plasmas

First-order finite-Larmor-radius fluid modeling of tearing and relaxation in a plasma pinch[a)]

J. R. King,[1,2,b)] C. R. Sovinec,[3] and V. V. Mirnov[1]

[1]*Department of Physics, University of Wisconsin-Madison, 1150 University Ave., Madison, Wisconsin 53706, USA*
[2]*Tech-X Corporation, 5621 Arapahoe Ave., Suite A Boulder, Colorado 80303, USA*
[3]*Department of Engineering-Physics, University of Wisconsin-Madison, 1500 Engineering Drive, Madison, Wisconsin 53706, USA*

Drift and Hall effects on magnetic tearing, island evolution, and relaxation in pinch configurations are investigated using a non-reduced first-order finite-Larmor-radius (FLR) fluid model with the nonideal magnetohydrodynamics (MHD) with rotation, open discussion (NIMROD) code [C.R. Sovinec and J. R. King, J. Comput. Phys. 229, 5803 (2010)]. An unexpected result with a uniform pressure profile is a drift effect that reduces the growth rate when the ion sound gyroradius (ρ_s) is smaller than the tearing-layer width. This drift is present only with warm-ion FLR modeling, and analytics show that it arises from ∇B and poloidal curvature represented in the Braginskii gyroviscous stress. Nonlinear single-helicity computations with experimentally relevant ρ_s values show that the warm-ion gyroviscous effects reduce saturated-island widths. Computations with multiple nonlinearly interacting tearing fluctuations find that $m = 1$ core-resonant-fluctuation amplitudes are reduced by a factor of two relative to single-fluid modeling by the warm-ion effects. These reduced core-resonant-fluctuation amplitudes compare favorably to edge coil measurements in the Madison Symmetric Torus (MST) reversed-field pinch [R. N. Dexter *et al.*, Fusion Technol. **19**, 131 (1991)]. The computations demonstrate that fluctuations induce both MHD- and Hall-dynamo emfs during relaxation events. The presence of a Hall-dynamo emf implies a fluctuation-induced Maxwell stress, and the simulation results show net transport of parallel momentum. The computed magnitude of force densities from the Maxwell and competing Reynolds stresses, and changes in the parallel flow profile, are qualitatively and semi-quantitatively similar to measurements during relaxation in MST. © *2012 American Institute of Physics*. [http://dx.doi.org/10.1063/1.3695346]

I. INTRODUCTION

Measurements in the Madison Symmetric Torus (MST)[1] reversed-field pinch (RFP) indicate effects beyond those captured by single-fluid-magnetohydrodynamics (MHD) modeling are significant.[2–4] These measurements often focus temporally on relaxation or "sawtooth" events where fluctuations are large. During these events, correlations of fluctuations induce emfs that flatten the current profile by driving poloidal current at $r \gtrsim 0.5a$, where a is the minor radius, and reducing the toroidal current in the core.[5] This dynamo action produces the associated conversion of poloidal magnetic flux to toroidal flux. The possibility of dynamo contributions beyond single-fluid MHD is evident through examination of the generalized Ohm's law,

$$\mathbf{E} = -\mathbf{v} \times \mathbf{B} + \frac{\mathbf{J} \times \mathbf{B}}{ne} - \frac{\nabla p_e}{ne} + \eta \mathbf{J} + \frac{m_e}{ne^2}\frac{\partial \mathbf{J}}{\partial t}, \quad (1)$$

where $\mathbf{E}$ is the electric field, $\mathbf{B}$ is the magnetic field, $\mathbf{v}$ is the center-of-mass velocity, p_e is the electron pressure, n is the plasma density, e is the electron charge, η is the resistivity, and m_e is the electron mass. In addition to the traditional

fluctuation-induced MHD-dynamo emf, $\langle \tilde{\mathbf{v}} \times \tilde{\mathbf{B}} \rangle$,[6] the use of the generalized Ohm's law allows for a Hall-dynamo emf, $\langle \tilde{\mathbf{J}} \times \tilde{\mathbf{B}} \rangle / ne$,[7] where the tilde and bracket indicate a fluctuating quantity and a flux surface average, respectively.

Laser-polarimetry measurements of the $m = 1$, $n = 6$ perturbed magnetic field, where m is the poloidal-mode number and n is the toroidal-mode number, show the Hall-dynamo emf induced from this mode is significant in the core of 400 kA standard MST plasmas during relaxation.[2,3] Additionally, magnetic probe measurements in 200 kA low-current plasmas demonstrate that Hall dynamo is important near the wall during relaxation.[4] Considerations of linear tearing modes,[8,9] the dominant long-wavelength instability in RFPs, show that the correlation $\langle \tilde{\mathbf{J}} \times \tilde{\mathbf{B}} \rangle$ vanishes with a single-fluid model.[10] Thus, self-consistent extended-MHD modeling is required to capture the effect of the Hall-dynamo emf as simply including an *ad-hoc* Hall emf with a single-fluid-MHD model is insufficient.

In addition to the Hall-dynamo emf, there is an associated force from the the Maxwell stress, $\langle \tilde{\mathbf{J}} \times \tilde{\mathbf{B}} \rangle$, which plays a role in fluctuation-induced momentum transport. However, Mach probe measurements during relaxation near the wall indicate that the fluctuation-induced force from the Reynolds stress, $m_i n \langle \tilde{\mathbf{v}} \cdot \nabla \tilde{\mathbf{v}} \rangle$, largely opposes the force from the Maxwell stress.[4] Even with near cancellation of these forces,

Rutherford-scattering measurements show that the resulting fluctuation-induced momentum transport considerably modifies the flow profiles.

Previous work shows single-fluid modeling gives a successful description of the dynamics of multiple nonlinearly interacting tearing modes, the RFP dynamo via the MHD-dynamo emf, and relaxation.[11–14] These results demonstrate a major strength of fluid modeling: the ability to run self-consistent, nonlinear computations in global domains approximating experimental-device configurations. Our intent is to build upon these results with extended-MHD. Our modeling captures first-order finite-Larmor-radius (FLR) effects through the generalized Ohm's law, Eq. (1), and the force from the ion gyroviscous stress in the momentum equation,

$$m_i n \frac{d\mathbf{v}}{dt} = \mathbf{J} \times \mathbf{B} - \nabla p - \nabla \cdot \Pi_{gv} - \nabla \cdot \nu m_i n \mathbf{W}, \quad (2)$$

where ν is the viscosity and $\mathbf{W}$ is the rate-of-strain tensor, $\mathbf{W} = \nabla \mathbf{v} + \nabla \mathbf{v}^T - (2/3)\mathbf{I}\nabla \cdot \mathbf{v}$. We use the fluid form of the ion gyroviscous stress,

$$\Pi_{gv} = \frac{m_i p_i}{4eB} [\hat{\mathbf{b}} \times \mathbf{W} \cdot (\mathbf{I} + 3\hat{\mathbf{b}}\hat{\mathbf{b}}) - (\mathbf{I} + 3\hat{\mathbf{b}}\hat{\mathbf{b}}) \cdot \mathbf{W} \times \hat{\mathbf{b}}], \quad (3)$$

where $\hat{\mathbf{b}} = \mathbf{B}/B$.[15] Compared to an inertial response at frequency ω, the gyroviscous stress scales as $\rho_i v_{Ti}/\omega L^2$, where $\rho_i = v_{Ti}/\omega_{ci}$ is the ion gyroradius and L is a characteristic gradient length. In this sense, it is a first-order FLR effect and important only with warm ions ($T_i \neq 0$).

Our results with this model are covered in Secs. III–V. In Sec. III, we review our study of the linear and nonlinear evolution of a single core-resonant tearing mode considered in more detail in Ref. 16. We find the growth of the tearing mode in the RFP is reduced by a drift response related to the gradient of the magnetic field and poloidal curvature when the drift frequency is on the order of the growth rate of the mode. Analytics show that this effect is manifest through contributions from ion gyroviscosity in the momentum equation. While the flux-surface average contribution from the ∇B and curvature drifts are small relative to diamagnetic drifts in tokamaks, they are dominant in pinch profiles. Growth rates and mode-rotation frequencies are derived for a heuristic dispersion relation using the ion-drift effects and a resistive-MHD Ohm's law. This dispersion relation is in agreement with numerical results in an intermediate drift regime before Kinetic-Alfvén wave (KAW) effects on the tearing mode are significant. Concerning the nonlinear evolution, we show that the saturated width of an island formed by tearing activity is reduced by contributions from the ion gyroviscous force when the ion gyroradius is significant. This reduction in the saturated width occurs for parameters that are experimentally relevant to modern RFPs.

We examine relaxation caused by the nonlinear interaction of multiple current-driven tearing fluctuations in Sec. IV. With experimentally relevant FLR parameters, two-fluid modeling shows the MHD- and Hall-dynamo emfs are comparable in amplitude and sign, and the combined emf acts to flatten the current profile during relaxation. In Sec. V, we make comparisons between our computations and MST measurements. The gyroviscous stabilization of the tearing perturbations described by our single-mode modeling is also present in our multiple-mode computations. Core-resonant-mode edge amplitudes from our two-fluid computations are reduced by a factor of two relative to single-fluid modeling and are comparable to laboratory measurements. During relaxation, the Hall-dynamo emf from the $m = 1$, $n = 6$ mode is similar to the laser-polarimetry measurement in sign and amplitude at the resonant surface. Near the edge, our computations are qualitatively similar to probe observations: there is a near cancellation of the fluctuation-induced forces from the Maxwell and Reynolds stresses. Finally, the computed fluctuation-induced modification of the parallel-flow profile is comparable to that observed with Rutherford scattering. Conclusions and a summary of future directions are discussed in Sec. VI.

II. MODEL

Our goal is to model tearing fluctuations during relaxation and the associated fluctuation-induced profile modifications. In order to correctly capture the KAW dynamics, we use a model with finite plasma compressibility. However, as we do not intend to model particle and thermal transport, we neglect Ohmic and viscous heating as well as anisotropic conductive heat flows in the temperature-evolution equation,

$$n\frac{\partial T}{\partial t} + n\mathbf{v} \cdot \nabla T = -\frac{2}{3}p\nabla \cdot \mathbf{v} + \frac{2}{3}\nabla \cdot \chi n \nabla T, \quad (4)$$

where the temperature (T) is related to the pressure through the ideal gas law, $p = nT$, and χ is a small thermal-diffusion coefficient. Correspondingly, we also neglect heat-flow contributions to ion gyroviscosity. The continuity equation,

$$\frac{\partial n}{\partial t} = -\nabla \cdot n\mathbf{v} + D_n\nabla^2 n, \quad (5)$$

is used to model the common plasma density as quasi-neutrality, $n \simeq n_i \simeq n_e$, is assumed. Here, D_n is a small particle diffusivity. The model is completed by Ampere's law without displacement current, $\mu_0\mathbf{J} = \nabla \times \mathbf{B}$ (μ_0 is the vacuum permeability), as is appropriate for modeling low-frequency dynamics, and Faraday's law, $\partial \mathbf{B}/\partial t = -\nabla \times \mathbf{E}$, in addition to the generalized Ohm's law, and the momentum, energy, and continuity equations, Eqs. (1) and (2), (4), and (5), respectively.

We evolve these equations with the initial-value nonideal magnetohydrodynamics with rotation, open discussion (NIMROD) code.[17] The two-fluid implicit leap-frog time-advance has been benchmarked with analytic tearing results in slab geometry without ion gyroviscosity and on plane-wave propagation and slab interchange with ion gyroviscosity, in addition to the cylindrical drift-analytics reviewed in Sec. III.[16,18,19] Unless otherwise noted, the computations use cylindrical geometry where the toroidal direction of experimental configurations is approximated by the cylindrical axial direction. The spatial discretization for multiple-mode

cases is a uniform radial-axial 240×60 finite-element mesh with polynomial-degree four elements and a Fourier decomposition with $0 \leq m \leq 5$ in the azimuthal direction.

The computations are initialized with the force-free ($\nabla p_{eq} = 0$) paramagnetic-pinch equilibrium[20] and small perturbations to excite physical instabilities. The pinch is an Ohmic equilibrium, $\nabla \times \mathbf{E}_{eq} = 0$, so it is suitable for studying fluctuation-induced emfs over resistive time scales. With uniform equilibrium-pressure, we focus on the dynamics of the current-driven tearing that dominates the core of standard RFP plasmas, and the diamagnetic-drift effects on the tearing mode are negligible.[21] The parallel-current profile ($\lambda = \mu_0 \mathbf{J} \cdot \mathbf{B}/B^2$) and safety factor ($q = rB_z/RB_\theta$) for the initial equilibrium fields in our multiple-mode computations are shown in Fig. 1. The configuration is characterized by the values of on-axis parallel current, $a\lambda(0) = 3.88$, aspect ratio $R/a = 3.03$, and plasma-β ($2\mu_0 nT/B^2$) of $\beta(0) = 0.1$. These choices result in multiple-mode computations with nearly constant normalized current, $\Theta = \langle B_\theta(a) \rangle V / \int B_z dV \simeq 1.6$, driven by a constant axial-loop voltage.

The choice of dissipation parameters is a compromise between MST experimental values and computationally tractable values. Their time-independent profiles are prescribed, and effects from temperature-dependent diffusivities are not considered in the computations presented here. The ratio of the resistive time to the Alfvén time, or the Lundquist number, is set to $S = \tau_R/\tau_A = 8 \times 10^4$, which is at least an order-of-magnitude smaller than in the MST core, where $\tau_R = a^2 \mu_0/\eta$ and $\tau_A = a\sqrt{m_i n \mu_0}/B$. Thermal and particle diffusivities are an order of magnitude smaller than magnetic diffusivity, $\chi \mu_0/\eta = D_n \mu_0/\eta = 0.1$. The magnetic-Prandtl number, $P_m = \nu \mu_0/\eta$, is unity and one tenth in our multiple and single tearing-mode studies, respectively. In order to suppress unphysical boundary-layer effects, the perturbed resistive and viscous terms use an edge-peaked diffusivity profile ($[1 + (\sqrt{20} - 1)(r/a)^{20}]^2$), and we refer to the value on-axis as characteristic.

Associated with the paramagnetic pinch equilibrium is a small ($\sim S^{-1}$) radially inward pinch flow. As the pinch flow is only a small part of the overall transport, and this overall transport is not being modeled, our model excludes the compressive effects of this flow. However, the density and pressure profiles are modified in our nonlinear computations through correlations of tearing fluctuations. For example, in our two-fluid multiple-mode computations, the on-axis density and temperature are reduced by 5%–10% and 2%–5%, respectively, and the core pressure profile remains relatively flat.

Extended-MHD analysis of tearing modes in slab geometry characterizes the fluid-decoupling parameter space by the ion-skin depth ($d_i = \sqrt{m_i/\mu_0 ne^2}$) and the plasma-$\beta$.[22,23] In general, decoupling effects associated with KAW-mediated tearing are significant if the ion sound gyroradius, $\rho_s = \sqrt{5\beta/6}d_i$, is larger than the tearing-layer width.[23–25] The tearing-layer width is set by the term in Ohm's law that breaks the frozen-in-flux condition: in the collisional/semi-collisional regime, where $d_e \ll \delta_\eta$, resistivity is responsible, and in the collisionless regime, where $d_e \gg \delta_\eta$, electron inertia is the relevant term.[22,26] Here, d_e is the collisionless electron skin depth ($\sqrt{m_e/\mu_0 ne^2}$) and δ_η is the resistive skin depth ($\sqrt{\eta/\mu_0 \gamma}$). Although we include electron inertia, $d_e = \min(5.21 \times 10^{-2} d_i, 9 \times 10^{-3} a)$, in our computations, our modeling is in the experimentally relevant (to MST) semi-collisional regime.

The results of our computations are typically reported in dimensionless form after normalization by τ_A, the minor radius or wavenumber where appropriate, and the magnitude of the toroidal field on axis, B_0. However, in Sec. V, to facilitate comparison with the MST measurements of Refs. 2–4, we convert our units using characteristic parameters $B_0 \simeq 0.4$ T and 0.2 T, and core temperatures of $T_i \simeq T_e \simeq 300$ eV and 200 eV during the 400 kA and 200 kA discharges, respectively. Other parameters common to these deuterium discharges are the minor and major radii: $a = 0.5$ m and $R = 1.5$ m, and $n \simeq 10^{19}$ m^{-3}. Thus, we estimate that $\rho_s = 0.02a$ and $0.04a$ for the low and high-current discharges, respectively. These values are comparable or slightly greater than an estimate of the tearing-layer width (using $\gamma \tau_A \simeq 10^{-3}$), so decoupling effects from KAW effects can be significant for linear modes.

III. REVIEW OF SINGLE-MODE STUDIES

Before discussing our nonlinear multiple-mode computations, we review the results of our linear and nonlinear studies of individual modes.[16] These single-mode computations
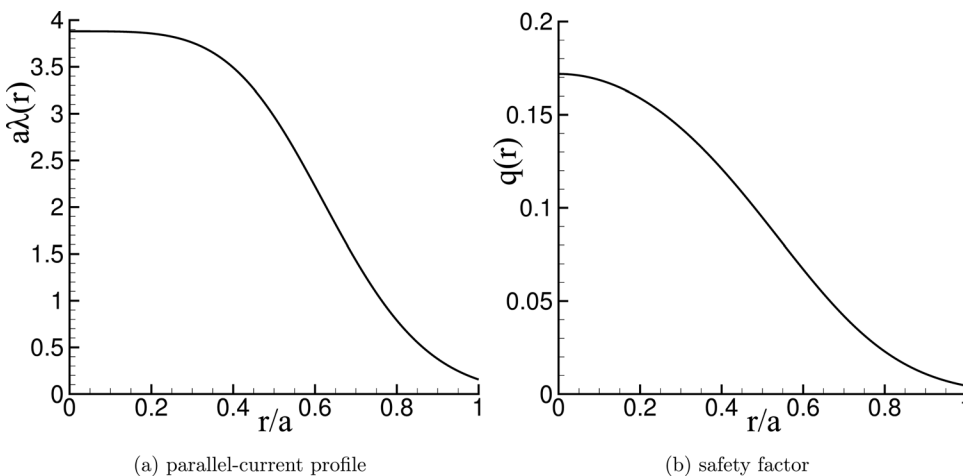

(a) parallel-current profile

(b) safety factor

FIG. 1. (a) Parallel-current profile ($a\lambda$) and (b) safety factor (q) as a function of radius for the paramagnetic-pinch equilibrium used in our multiple-mode computations.
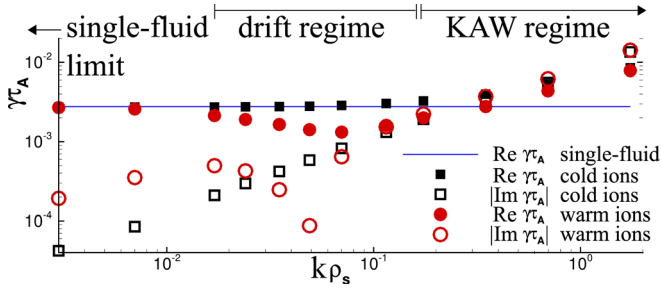
FIG. 2. Linear growth (Re $\gamma\tau_A$) and mode-rotation rates (Im $\gamma\tau_A$) for an $m = 1$ core mode with single-fluid, cold-ion and warm-ion models.

TABLE I. Saturated-island width from cold- and warm-ion modeling with varying values of $k\rho_s$ and S.

$k\rho_s$	S	W/a (cold)	W/a (warm)
Single fluid	5000	0.36	
0.035	5000	0.36	0.36
0.17	5000	0.36	0.24
0.17	8×10^4	0.36	0.24
0.70	5000	0.36	0.21

consider a paramagnetic pinch with $a\lambda(0) = 3.3$ to approximate a relaxed-RFP core. The resonant mode is then equivalent to a $m = 1$, $n = 6$ mode is MST, with $ka = 3.5$ and a tearing stability parameter of $\Delta'a = 15$.[8] Our parameter space scan varies ρ_s through d_i while holding β constant at 0.1. Additionally, for each ρ_s value we run two computations: cold-ion ($T_i = 0$, thus no gyroviscosity) and warm-ion ($T_i = T_e$) modeling. Thus, we are able to distinguish effects of the generalized Ohm's law from those of ion gyroviscosity.

The computed linear growth and mode-rotation rates as a function of $k\rho_s$ are shown in Fig. 2 for three models: single-fluid, cold-, and warm-ion. These computations have three regimes. In the limit of small $k\rho_s$ where single-fluid MHD is valid, all models converge to the same growth rate with vanishing rotation. On the right side of the figure, $k\rho_s$ is larger than the tearing-layer width, and the warm- and cold-ion two-fluid models have enhanced growth rates as expected in the KAW-mediated tearing regime.[22,23] In this regime, the dynamics of the mode are determined by the electron fluid, which potentially allows the first-order FLR model to be qualitatively descriptive when the ion gyroradius is not a small parameter. The warm- and cold-ion mode-rotation at large $k\rho_s$ is shown to be a cylindrical two-fluid effect in Ref. 27. Finally, there is an unexpected intermediate-$k\rho_s$ regime, where warm-ion growth rates are suppressed relative to both the cold-ion and single-fluid modeling.

Analytics provide insight into the relevant physics in the intermediate-$k\rho_s$ regime. We consider the gyroviscous contributions to the parallel-vorticity equation with a flux representation for the perturbed magnetic field,

$$\tilde{\mathbf{B}} = \nabla\tilde\psi \times \mathbf{B}_0 + \tilde{B}_\parallel \hat{\mathbf{b}}_0, \qquad (6)$$

and a nearly incompressible stream-function representation for the velocity,

$$\tilde{\mathbf{v}} = \hat{\mathbf{b}}_0 \times \nabla\tilde\phi + \tilde{v}_\parallel \hat{\mathbf{b}}_0. \qquad (7)$$

We then apply tearing ordering to the flow where the small ratio of the tearing-layer width relative to k^{-1} allows us to consider each radial derivate of $\tilde\phi$ as order ϵ^{-1}, where ϵ is a small parameter (thus, if $\tilde\phi \sim \mathcal{O}(1)$, then $\tilde\phi' \sim \mathcal{O}(\epsilon^{-1})$, $\tilde\phi'' \sim \mathcal{O}(\epsilon^{-2})$, etc.). The tearing-ordered parallel-vorticity equation without a pressure-profile gradient is then

$$(\gamma - i\omega_{*gv})\tilde\phi'' = -v_A^2 ik_\parallel \tilde\psi'', \qquad (8)$$

where

$$\omega_{*gv} = \frac{k_\perp}{m_i n_0} \frac{p_{i0}}{\omega_{ci0}} \left(\frac{3}{2} \frac{B_{0\theta}^2}{B_0^2 r} - \frac{B_0'}{B_0} \right) \qquad (9)$$

is the gyroviscous contribution.[16] The tearing-ordered gyroviscous torque produces a drift term that represents contributions from poloidal curvature ($B_\theta^2/B_0^2 r$) and magnetic-field gradient.

Combining the parallel-vorticity equation, Eq. (8), with the single-fluid resistive flux-evolution equation produces a coupled-set of equations that describe the tearing layer when KAW effects are not significant. Solving for a heuristic dispersion relation for the tearing mode in the intermediate-$k\rho_s$ drift regime one finds

$$\gamma^4(\gamma - i\omega_{*gv}) = \gamma_{MHD}^5, \qquad (10)$$

where γ_{MHD} is the resistive-MHD tearing growth rate. Detailed comparison with our computations finds this dispersion relation accurately describes the growth and rotation rates of our warm-ion computations in the single-fluid and intermediate regimes until KAW-mediated tearing becomes significant.[16]

The poloidal flux and magnetic field strength are shown for characteristic tokamak and RFP toroidal equilibria in

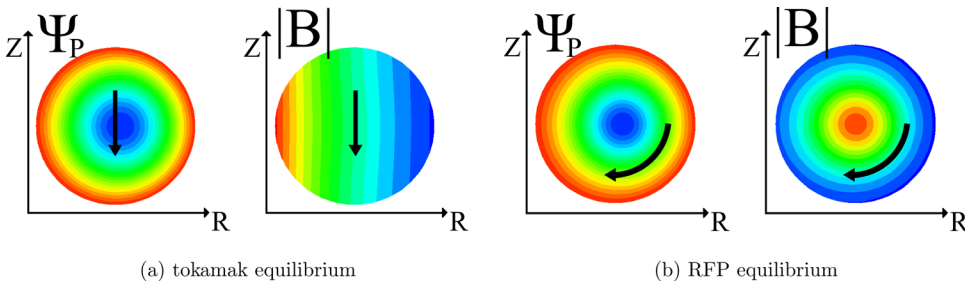(a) tokamak equilibrium

(b) RFP equilibrium

FIG. 3. Poloidal flux and the amplitude of the magnetic field for characteristic (a) tokamak and (b) RFP toroidal equilibria. The arrow indicates the poloidal projection of the dominant ∇B and curvature drift for each equilibrium.
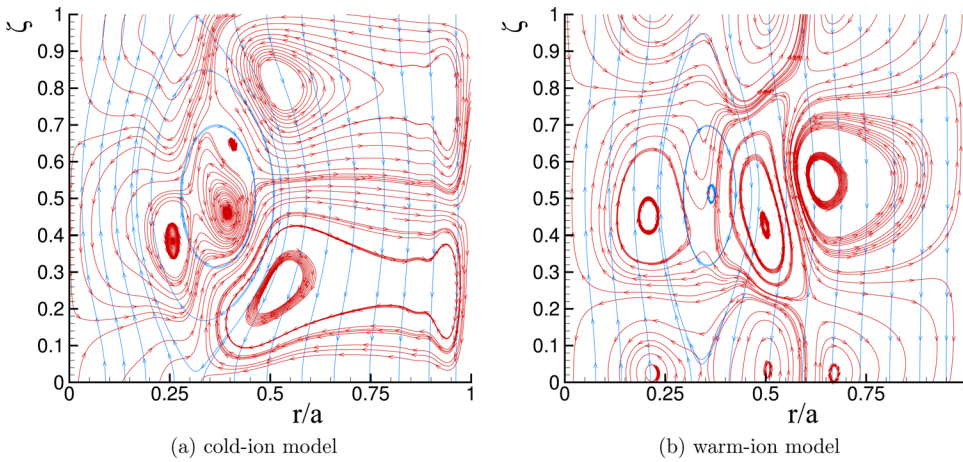
(a) cold-ion model

(b) warm-ion model

FIG. 4. A projection of the tearing-mode magnetic (blue, light grey, single island at $r_s = 0.35a$) and ion-flow (red, dark grey) structures onto a representative helical surface from single-island (a) cold- and (b) warm-ion modeling.

Fig. 3 along with an arrow, which indicates the poloidal projection for the dominant ∇B and curvature drifts. These equilibria are solutions of the Grad-Shafranov equation produced with the NIMEQ code.[28] The dominant ∇B and curvature drifts in tokamaks are not aligned with flux surfaces where tearing modes are resonant. Thus, after a flux-surface average, these drifts are relatively small. However, in the RFP, the drifts from ∇B and the relatively large poloidal curvature are roughly aligned with the tearing-mode resonant surfaces and are oriented along the direction of variation of the mode. As electrons and ions drift in opposite directions, this separation of fluids shears the dynamics and has a stabilizing influence on the mode.

Nonlinear single-mode computations model the tearing evolution through a Rutherford stage[29] to near saturation. Table I shows the computed saturated-island width for a series of $k\rho_s$ and Lundquist-number values. We have

confirmed that the resulting widths are not modified in the limit of vanishing isotropic viscosity. Our cold-ion computations find the saturated-island width is insensitive to the use of a generalized Ohm's law, a result supported by the analytics of Ref. 30. However, warm-ion modeling shows the saturated-island width to be reduced at values of $k\rho_s$ relevant to MST core-resonant tearing modes. Analysis of the forces retarding the island growth demonstrates the importance of the ion-gyroviscous force in reducing the width at saturation.[16] Here, the magnetic-field profile, hence the associated ∇B and curvature drifts, is not significantly modified through nonlinear effects in the presence of an island, unlike the diamagnetic drift and pressure profile, which are subject to transport effects.[31,32]

In Fig. 4, the cold- and warm-ion single-helicity island structures are projected onto a perpendicular helical surface for $k\rho_s = 0.17$. With a cold-ion model, the ion vorticies

(a) Magnetic spectral energies
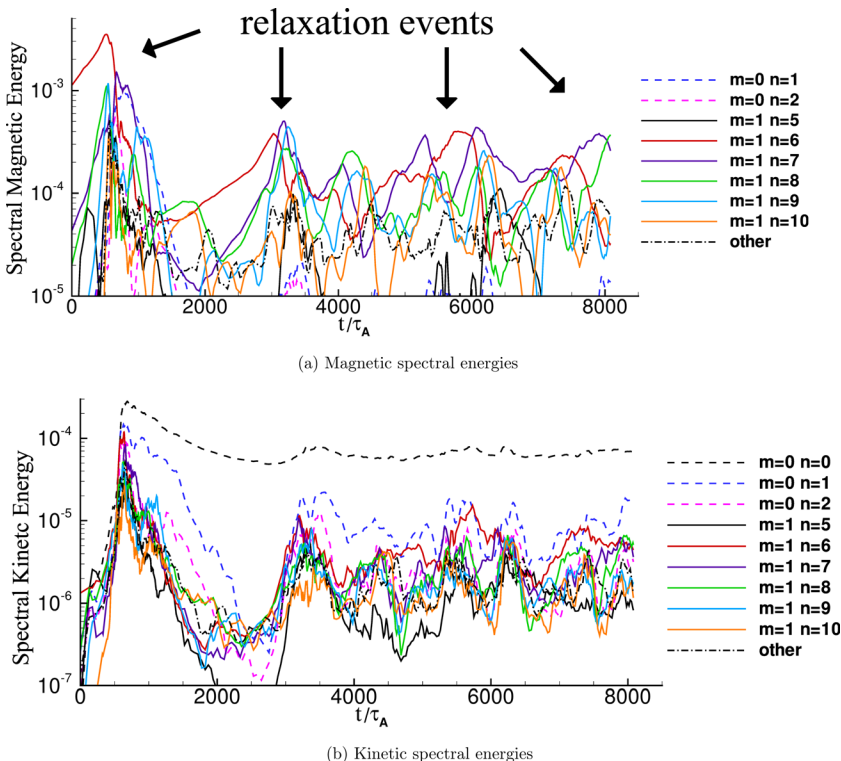

(b) Kinetic spectral energies

FIG. 5. (a) Magnetic and (b) kinetic spectral energies as a function of time from our extended-MHD computation. Values are normalized such that the mean magnetic energy is approximately 1. The mean magnetic energy has temporal variations of less than 1% in the computation.

(a) Zero-β single-fluid model   (b) Finite-β single-fluid model
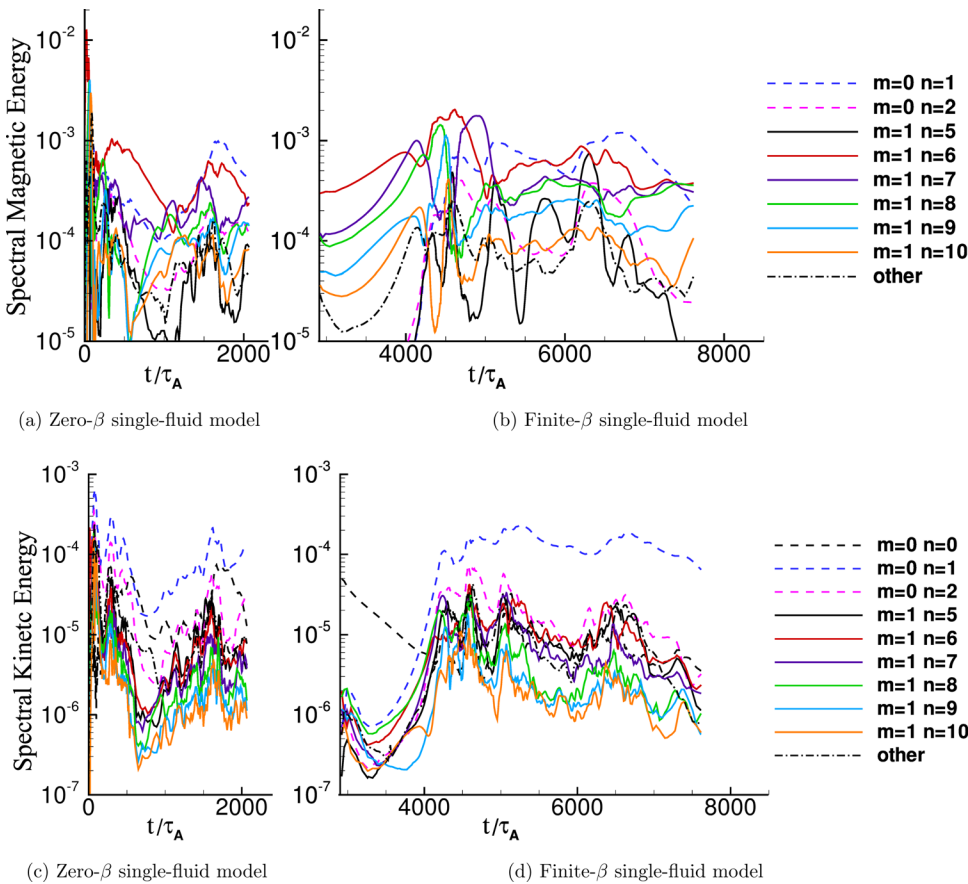
FIG. 6. (a-b) Magnetic and (c-d) kinetic spectral energies as a function of time from our single-fluid computations. Values are normalized such that the mean magnetic energy is approximately 1. The mean magnetic energy has temporal variations of less than 3% in the computations. Note the vertical-axis scale differs from Fig. 5.

(c) Zero-β single-fluid model   (d) Finite-β single-fluid model

IV. MULTIPLE-MODE COMPUTATIONS

We now discuss results from multiple-mode modeling of RFP relaxation. The nonlinearly interacting current-driven-tearing fluctuations self-consistently relax the profile and cause the edge toroidal magnetic field to reverse relative to the initial paramagnetic-pinch equilibrium, as in RFP experiments. We consider three computations: one with the full warm-ion extended-MHD model with $\rho_s = 0.05a$ in the plasma core ($0 \leq t \leq 8081\tau_A$), one with a zero-β resistive-MHD model ($0 \leq t \leq 2065\tau_A$), and one with a finite-β (0.1) resistive-MHD model initialized from the extended-MHD state ($2922\tau_A \leq t \leq 7616\tau_A$). We refer to the first as two-fluid and the latter two as single-fluid, and all computations have identical shared characteristic parameters.

The spectral magnetic and kinetic energies (Fig. 5) provide a more detailed overview of the dynamics in our two-fluid computation. There is a large initial-relaxation event at $t \simeq 650\tau_A$ as characterized by a spike in the magnetic- and kinetic-fluctuation energies. After this event, the fluctuation energies are lower, indicating partial stabilization of the pro-

advect flux radially into the magnetic x-point and then to the magnetic o-point to sustain the saturated island against magnetic diffusion. The dominant flow structure is significantly modified with a warm-ion model as the dominant ion eddies are out of phase with those that support magnetic reconnection. In fact, analysis shows that these out-of-phase eddies are responsible for the ion-gyroviscous force that opposes the force driving the island growth.[16]

file. There are additional relaxation events as the computation progresses ($t \simeq 3250\tau_A$, $t \simeq 5800\tau_A$, and $t \simeq 7900\tau_A$), however, the amplitude of the fluctuations remains much smaller than the initial event. The subsequent relaxation produces significant $m = 1$ and $6 \leq n \leq 8$ activity, but only during the initial event are $m = 0$ modes excited to large amplitude. Analysis of $m = 0$ energy drive and gyroviscous forces shows that the suppressed $m = 0$ amplitude in the latter events is not the result of a gyroviscous stabilization but rather the absence of nonlinear drive from the $m = 1$ fluctuations.

For comparison, the spectral energies from our single-fluid computations are shown in Fig. 6. The initial relaxation event with a zero-β resistive-MHD model is immediate and associated with large magnetic mode amplitudes at $t \simeq 100\tau_A$. A second relaxation event occurs at $t \simeq 1600\tau_A$. The finite-β resistive-MHD computation is initialized from
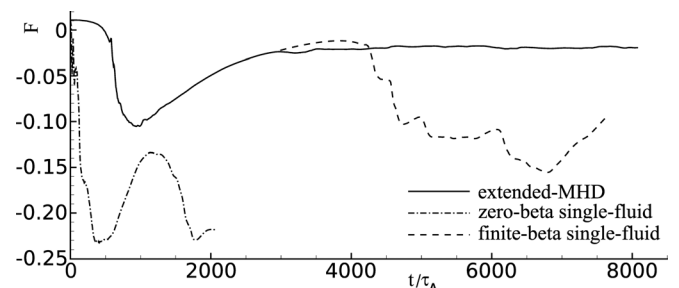

FIG. 7. Field-reversal parameter ($F = \langle B_z(a) \rangle V / \int B_z dV$) for our single-fluid and extended-MHD computations as a function of time.
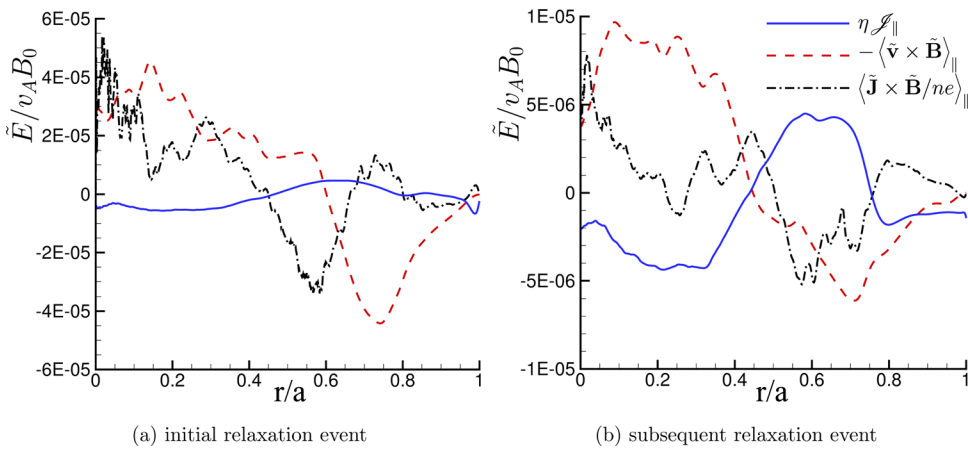
FIG. 8. Time-averaged dynamo emfs and current-profile modification during the (a) initial ($612\tau_A \leq t \leq 684\tau_A$) and (b) subsequent ($3178\tau_A \leq t \leq 3332\tau_A$) relaxation events from the extended-MHD computations (vertical-axis scales differ).

(a) initial relaxation event

(b) subsequent relaxation event

the two-fluid state and exhibits slow growth of the magnetic mode energies from $3000\tau_A \lesssim t \lesssim 4000\tau_A$, as well as a steady decrease in the $m = 0$, $n = 0$ kinetic energy. The first relaxation event of the finite-β computation occurs near $t \simeq 4650\tau_A$, and has magnetic mode energies approximately a factor of four larger than the analogous two-fluid event at $t \simeq 3250\tau_A$.

The reversal parameter ($F = \langle B_z(a)\rangle V / \int B_z dV$) from our computations is plotted as a function of time in Fig. 7. From comparison with spectral energies (Figs. 5 and 6), precipitous decreases in the reversal parameter are associated with the increased $m = 0$, $n = 1$ magnetic activity during some relaxation events.

Figure 8 shows the average parallel dynamo emfs and associated profile modification relative to the initial paramagnetic-pinch equilibrium ($\vec{\mathscr{J}}_0 \equiv \langle \mathbf{J}\rangle - \mathbf{J}_{eq}$) during the initial ($612\tau_A \leq t \leq 684\tau_A$) and subsequent ($3178\tau_A \leq t \leq 3332\tau_A$) relaxation events of the two-fluid case. During both events, the combined dynamo emf acts to flatten the current profile by driving parallel current in the edge, and reducing it in the core. The MHD- and Hall-dynamo emfs are of comparable amplitude. The measurements of Ref. 3 show a fivefold difference in the amplitude of the $m = 1$, $n = 6$ Hall dynamo between deeply reversed and marginally reversed MST discharges with reversal parameters of $F = -0.22$ and $F = 0$, respectively. Our results are qualitatively similar as the initial event has

$F \simeq -0.11$ and a Hall dynamo emf that is approximately a factor of four to eight larger than during the subsequent relaxation event with $F \simeq -0.02$.

It is instructive to compare the two-fluid dynamo emfs (Fig. 8) with the single-fluid result (Fig. 9) during relaxation events that occur after a shared initial condition: the initial ($61\tau_A \leq t \leq 138\tau_A$) and subsequent ($4600\tau_A \leq t \leq 4701\tau_A$) single-fluid events. During the zero-β single-fluid initial relaxation event (Fig. 9(a)), the MHD-dynamo emf is comparable to the two-fluid combined dynamo emf (Fig. 8(a)), and produces a similar global redistribution of current. Comparison of the subsequent relaxation event leads to the same conclusion: the MHD-dynamo emf during the finite-β relaxation event (Fig. 9(b)) is comparable to the two-fluid combined dynamo emf (Fig. 8(b)), and the current profile redistribution is similar.

V. COMPARISON WITH EXPERIMENTAL MEASUREMENTS

Next, we compare the results of our computations with measurements from MST. Our intention is not a full validation of the model, but rather to illustrate experimentally relevant effects captured by the FLR model that are not present with a resistive-MHD model. In Sec. VI, we discuss extensions to the FLR model which should be investigated before it is reasonable to pursue validation.
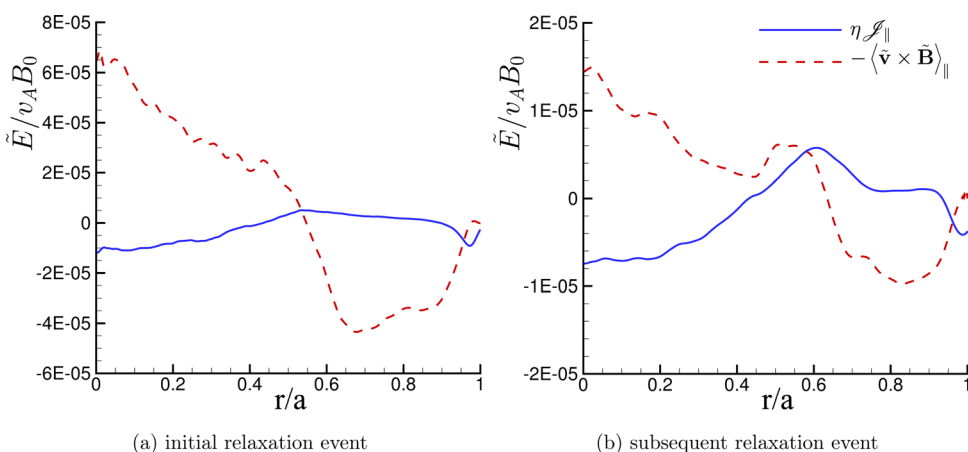

FIG. 9. Time-averaged dynamo emfs and current-profile modification during the (a) initial ($61\tau_A \leq t \leq 138\tau_A$, zero β) and (b) subsequent ($4600\tau_A \leq t \leq 4701\tau_A$, finite β) relaxation events from the single-fluid computations (vertical-axis scales differ).

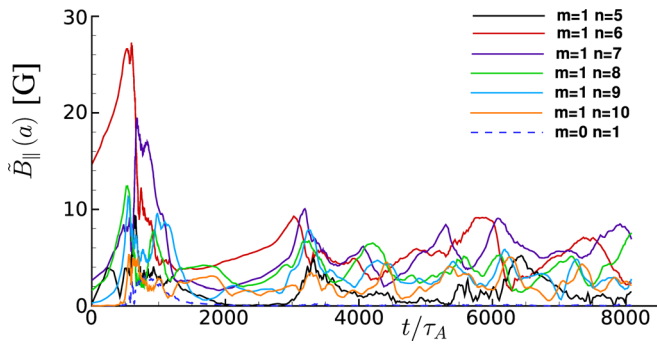(a) initial relaxation event

(b) subsequent relaxation event

FIG. 10. The amplitude of $\tilde{B}_{\parallel}(a)$ of the $m=0$, $n=1$ and the $m=1$, $5 \leq n \leq 10$ modes as a function of time from our two-fluid computation. Units appropriate for 400 kA MST discharges have been applied.

A. Edge mode amplitudes

Figure 10 shows the computed amplitude of $\tilde{B}_{\parallel}(a)$ ($\simeq \tilde{B}_{\theta}(a)$), evaluated for 400 kA parameters and decomposed by mode as a function of time. Similar to the behavior of the magnetic-fluctuation energies, the amplitude of $\tilde{B}_{\parallel}(a)$ is much larger during the initial relaxation event relative to the subsequent evolution. We compare the computed result to the measured $\tilde{B}_{\theta}(a)$ shown in Fig. 10 of Ref. 3, where the experimental discharges are somewhat more strongly driven ($\Theta \simeq 1.7$) than our computations ($\Theta \simeq 1.6$). The measurements distinguish relaxation events with deep ($F = -0.22$) and marginal ($F = 0$) reversal. During the strongly driven initial ($F \simeq -0.11$) event from our two-fluid computation, the maximum core-resonant-fluctuation edge amplitude (26 G computed) is 85% larger than that measured during $F = -0.22$ discharges (14 G measured). However, a comparison of the core-resonant amplitudes computed with the two-fluid model during the subsequent relaxation events, where $F \simeq -0.02$, with the $F = 0$ measurements is more favorable. Both the two-fluid computation and experimental measurements find the maximum core-resonant-fluctuation edge amplitude is approximately 10 G during relaxation and 5 G between events.

The comparable single-fluid computations (Fig. 11) produce core-resonant-fluctuation edge amplitudes approximately twice the size of the warm-ion FLR result. During the

initial relaxation event, the zero-β single-fluid model leads to a maximum amplitude of 50 G, and during the subsequent evolution both the zero-β and finite-β single-fluid models have a maximum amplitude of 15–20 G during relaxation and 8–10 G between events. Thus, the core-resonant-fluctuation edge amplitudes predicted by the two-fluid model are closer to those measured in MST than the comparable single-fluid predictions, and this provides indirect support that the gyroviscous stabilization of core-resonant fluctuations described in Sec. III may be present in experiment. An alternative explanation of the relatively reduced measured fluctuation amplitudes may be the fluctuation scaling of $S^{-1/5}$ computed with a single-fluid model,[14] given the discrepancy between the model and experimental dissipation parameters. After the first relaxation event, our two-fluid computations do not produce the $m=0$ dynamics measured to be 5–10 G during relaxation in MST. In this aspect, the single-fluid modeling is more representative of the edge $m=0$ dynamics.

B. Hall-dynamo emf

The contributions from specific modes to the Hall- and MHD-dynamo emfs are significant near each mode resonant surface, as shown in Fig. 12. Each mode tends to flatten the current profile around its resonant surface by reducing the current on the radially inward side and driving current on the radially outward side, resulting in a collective global redistribution of the parallel-current profile.

We compare the result of the computations during the initial relaxation to the $m=1$, $n=6$ Hall-dynamo emf inferred from Faraday-rotation measurements, as both have significant $m=0$ activity and thus strongly coupled core modes. The measured $m=1$, $n=6$ Hall-dynamo emf, shown in Figs. 7 and 8 of Ref. 3, has a similar amplitude to the computed result at the resonant surface: 40 V/m. However, the experimental $m=1$, $n=6$ Hall-dynamo emf is radially localized to the resonant surface and strictly positive, unlike the computed profile. A more detailed comparison, where the computed Hall-dynamo emf is decomposed by contributions from components of the perturbed current and magnetic field will be presented in a future paper.
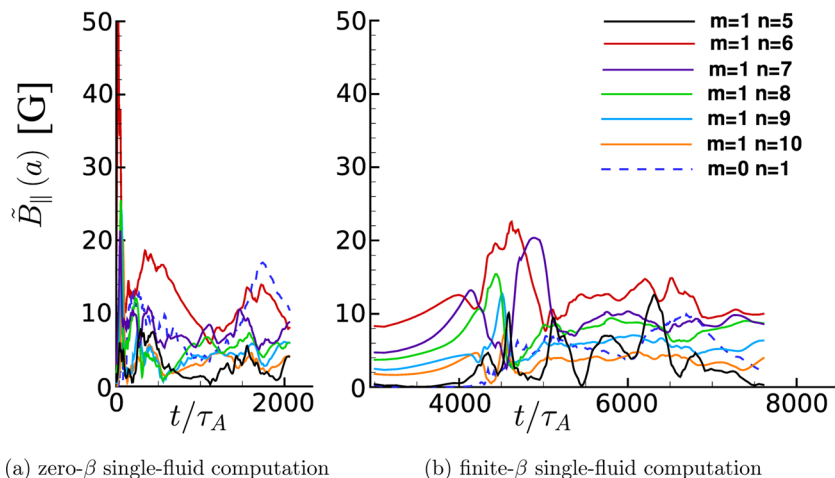

(a) zero-β single-fluid computation

(b) finite-β single-fluid computation

FIG. 11. The amplitude of $\tilde{B}_{\parallel}(a)$ of the $m=0$, $n=1$ and the $m=1$, $5 \leq n \leq 10$ modes as a function of time from our (a) zero- and (b) finite-β single-fluid computations. Units appropriate for 400 kA MST discharges have been applied. Note the vertical-axis scale differs from Fig. 10.

(a) Hall-dynamo emf contributions by mode
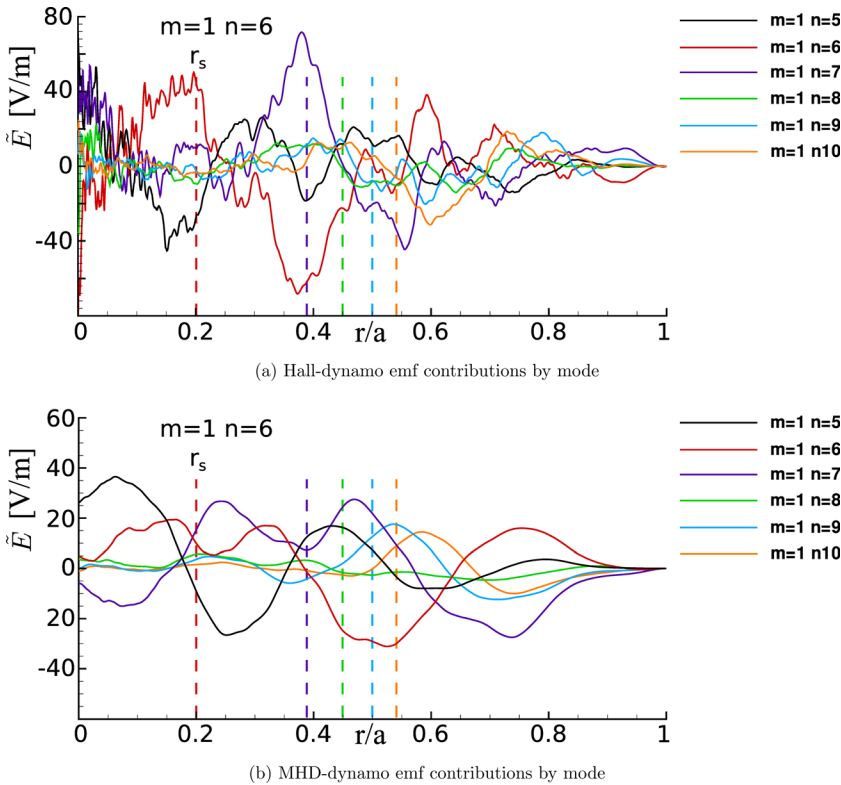

(b) MHD-dynamo emf contributions by mode

FIG. 12. Time-averaged contributions to the (a) Hall- and (b) MHD-dynamo emfs from individual modes during the initial relaxation event ($612\tau_A \leq t \leq 684\tau_A$). Mode resonant surfaces are indicated by the dashed lines. Units are evaluated for 400 kA MST discharges.

C. Fluctuation-induced forces

Associated with the Hall-dynamo emf is a force from the fluctuation-induced Maxwell stress. This force, along with the force from the fluctuation-induced Reynolds stress, has been measured with edge probes in MST. As shown in Figs. 6 and 7 of Ref. 4, these forces are significant near relaxation events, and tend to oppose each other with radially varying structure.

Again, we compare the measurements to the initial relaxation in the computation, as both have significant core-mode coupling and associated $m = 0$ activity. Figure 13(a) demonstrates that similar to the measurements, the forces from the Maxwell and Reynolds stresses computed with the two-fluid model are also largely opposed with radial variation in their structure. However, the computed magnitude of the forces in the edge is approximately a factor of three smaller than the measurements. The mean parallel forces from zero-β single-fluid modeling (Fig. 13(b)) do reproduce

this behavior: the force from the Maxwell stress nearly vanishes, and the force from the Reynolds stress does not have global structure.

D. Flow profile modification

Both experimental measurements and our two-fluid model find that fluctuation-induced forces modify the parallel-flow profile during relaxation. Our computations begin with no mean flow, thus the flow profile after the initial relaxation event, shown in Fig. 14, represents the flow driven by the fluctuation-induced forces. The computed two-fluid flow-profile modification is similar to that measured in experiment by Rutherford scattering as indicated in the figure by stars inferred from Fig. 4 of Ref. 4. The fluctuation-induced forces generate mean flow parallel to the magnetic field in the plasma core, and anti-parallel to the magnetic field mid-radius. The comparable single-fluid computation does not produce significant modifications to the parallel-flow profile.

(a) Two-fluid model, $612\tau_A \leq t \leq 684\tau_A$

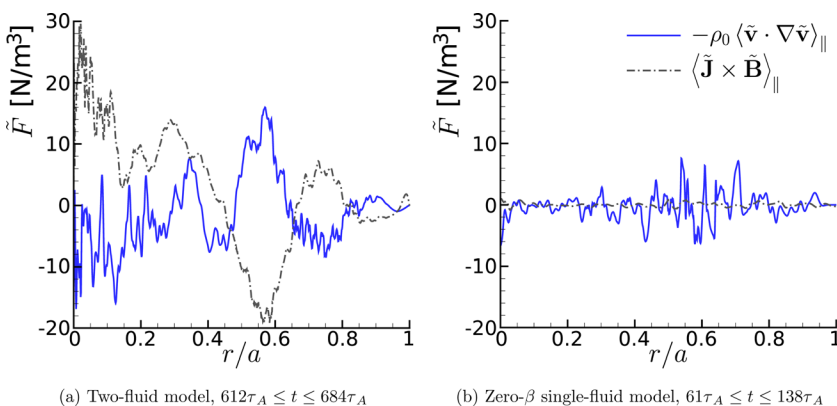(b) Zero-β single-fluid model, $61\tau_A \leq t \leq 138\tau_A$

FIG. 13. Time-averaged mean parallel fluctuation-induced forces from the Maxwell and Reynolds stresses during the initial relaxation events for the (a) two-fluid and (b) zero-β single-fluid models. Units are evaluated for 200 kA MST discharges.
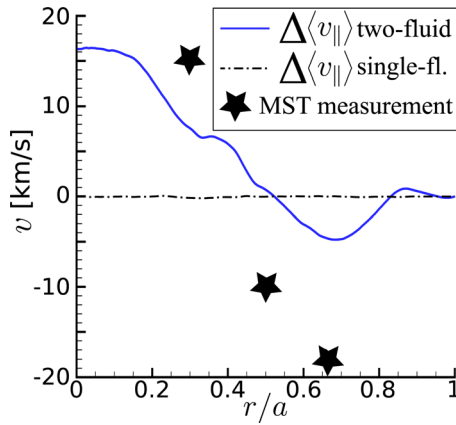
FIG. 14. Computed flow profile generated during the two-fluid initial relaxation event, $612\tau_A \leq t \leq 684\tau_A$ (solid line), and the single-fluid initial relaxation event, $61\tau_A \leq t \leq 138\tau_A$ (dot-dashed line). Units are evaluated for 200 kA MST discharges. Stars indicate relaxation-induced changes to the parallel flow inferred from Fig. 4 of Ref. 4.

VI. DISCUSSION AND CONCLUSION

Our computations demonstrate the importance of first-order FLR corrections when modeling RFP discharges. With respect to linear tearing, we show there is an ion drift from ∇B and curvature, manifest in the model through ion gyroviscosity, which can have a stabilizing influence on tearing. When ρ_s is larger than the tearing-layer width, the expected KAW-mediation occurs and the electron dynamics dominate. Thus, although our extended-MHD model contains only first-order FLR corrections, it may be qualitatively descriptive of modes without a strictly small ion gyroradius. Concerning the nonlinear saturation of a single tearing mode with a warm-ion model, we find the force from ion gyroviscosity opposes the forces driving the island, leading to saturation at smaller width than predicted by resistive-MHD modeling.

Although our multiple-mode modeling uses both single-fluid and extended-MHD, it does not perform an extensive parameter scan. Using our single-mode cases to estimate experimental regimes, we expect gyroviscous stabilization becomes significant when $k\rho_i \gtrsim 0.02$. For standard MST discharges (400 kA and $B_0 \simeq 0.4$ T), we estimate that a mode resonant at $r_s = 0.35a$ is subject to gyroviscous stabilization at $T_i \gtrsim 60$ eV. With respect to KAW-mediation, in general, we expect that it is significant when ρ_s is larger than the tearing layer width: $l/a \simeq \Delta'(S\gamma\tau_A)^{-1}$ for small-Δ' modes.[22,23,26] Using Spitzer resistivity and estimating $\Delta' a \simeq 10$ and $\gamma\tau_A \simeq 10^{-3}$ for standard MST discharges, this condition is met at $T_e \gtrsim 200$ eV with negligible ion temperature, $T_e \gtrsim 175$ eV with $T_i = 100$ eV, and $T_e \gtrsim 160$ eV with $T_i = 200$ eV.

Self-consistent nonlinear multiple-mode first-order FLR RFP modeling demonstrates the importance of the Hall dynamo-emf during relaxation at experimentally relevant parameters. Our extended-MHD model qualitatively reproduces effects measured in the experiment that are not present with single-fluid modeling: reduced core-resonant mode amplitudes from the influence of gyroviscosity, the aforementioned Hall-dynamo emf, fluctuation-induced forces from the Maxwell and Reynolds stresses, and significant modifications to the parallel-flow profile during relaxation. However, our extended-MHD modeling does not repetitively generate the $m = 0$ mode dynamics observed during standard MST discharges. Before detailed validation of the model can be made, investigation of relaxation with a realistic pressure profile, which would include nontrivial interchange and diamagnetic effects as well a more realistic ρ_s profile, should be attempted. As pressure gradients in the experiment are typically largest near the edge of the plasma, we expect the $m = 0$ dynamics would be modified. These computations can be performed while decreasing the dissipation parameters to more accurately match experimental conditions. Another area of future study is the comparison of two-fluid relaxation theories, for example Refs. 33–35, which predict coupled current- and flow-profile changes from relaxation as observed in both experiment and our computations.

[1]R. N. Dexter, D. W. Kerst, T. W. Lovell, S. C. Prager, and J. C. Sprott, Fusion Technol. **19**, 131 (1991).

[2]W. X. Ding, D. L. Brower, D. Craig, B. H. Deng, G. Fiksel, V. Mirnov, S. C. Prager, J. S. Sarff, and V. Svidzinski, Phys. Rev. Lett. **93**, 045002 (2004).

[3]W. X. Ding, D. L. Brower, B. H. Deng, A. F. Almagri, D. Craig, G. Fiksel, V. Mirnov, S. C. Prager, J. S. Sarff, and V. Svidzinski, Phys. Plasmas **13**, 112306 (2006).

[4]A. Kuritsyn, G. Fiksel, A. F. Almagri, D. L. Brower, W. X. Ding, M. C. Miller, V. V. Mirnov, S. C. Prager, and J. S. Sarff, Phys. Plasmas **16**, 055903 (2009).

[5]S. Ortolani and D. D. Schnack, *Magnetohydrodynamics of Plasma Relaxation* (World Scientific Pub Co. Inc., 1993).

[6]H. K. Moffatt, *Magnetic Field Generation in Electrically Conducting Fluids* (Cambridge University Press, Cambridge, England, 1978).

[7]R. A. Nebel, in *Proceedings of the Physics of Alternative Magnetic Confinement Schemes*, edited by S. Ortoloni and E. Sindoni (Societa Italiana di Fisica, Editrice Compositori, Bologna, Italy, 1991), p. 611.

[8]H. P. Furth, J. Killeen, and M. N. Rosenbluth, Phys. Fluids **6**, 459 (1963).

[9]B. Coppi, J. M. Greene, and J. L. Johnson, Nucl. Fusion **6**, 101 (1966).

[10]V. V. Mirnov, C. C. Hegna, and S. C. Prager, Plasma Phys. Rep. **29**, 566 (2003).

[11]D. D. Schnack, E. J. Caramana, and R. A. Nebel, Phys. Fluids **28**, 321 (1985).

[12]J. A. Holmes, B. A. Carreras, P. H. Diamond, and V. E. Lynch, Phys. Fluids **31**, 1166 (1988).

[13]Y. L. Ho and G. G. Craddock, Phys. Fluids **3**, 030721 (1991).

[14]S. Cappello and D. Biskamp, Nucl. Fusion **36**, 571 (1996).

[15]P. J. Catto and A. N. Simakov, Phys. Plasmas **11**, 90 (2004).

[16]J. R. King, C. R. Sovinec, and V. V. Mirnov, Phys. Plasmas **18**, 042303 (2011).

[17]C. R. Sovinec, A. H. Glasser, T. A. Gianakon, D. C. Barnes, R. A. Nebel, S. E. Kruger, S. J. Plimpton, A. Tarditi, M. S. Chu, and NIMROD Team, J. Comput. Phys. **195**, 355 (2004).

[18]C. R. Sovinec and J. R. King, J. Comput. Phys. **229**, 5803 (2010).

[19]P. Zhu, D. D. Schnack, F. Ebrahimi, E. G. Zweibel, M. Suzuki, C. C. Hegna, and C. R. Sovinec, Phys. Rev. Lett. **101**, 085005 (2008).

[20]D. C. Robinson, Nucl. Fusion **18**, 939 (1978).

[21]B. Coppi, Phys. Fluids **7**, 1501 (1964).

[22]V. V. Mirnov, C. C. Hegna, and S. C. Prager, Phys. Plasmas **11**, 4468 (2004).

[23]E. Ahedo and J. J. Ramos, Plasma Phys. Controlled Fusion **51**, 055018 (2009).

[24]L. Zakharov and B. Rogers, Phys. Fluids B **4**, 3285 (1992).

[25]B. N. Rogers, R. E. Denton, J. F. Drake, and M. A. Shay, Phys. Rev. Lett. **87**, 195004 (2001).

[26]J. F. Drake and Y. C. Lee, Phys. Fluids **20**, 1341 (1977).

[27]V. V. Mirnov, C. C. Hegna, S. C. Prager, C. R. Sovinec, and H. Tian, "Two fluid dynamo and edge-resonant $m = 0$ tearing instability in reversed field pinch," in Proceedings of the 21st IAEA Conference **TH/P3-18**, Chendu, China, October 2006. Available at: http://www-naweb.iaea.org/napc/physics/FEC/FEC2006/html/node186.htm#36729

[28]E. C. Howell and C. R. Sovinec, "NIMEQ: MHD equilibrium solver for NIMROD," APS Meeting Abstracts (2008).

[29]P. H. Rutherford, Phys. Fluids **16**, 1903 (1973).

[30]S. Cappello, D. Bonfiglio, D. F. Escande, S. C. Guo, I. Predebon, F. Sattin, M. Veranda, P. Zanca, C. Angioni, L. Chacon, J. Q. Dong, X. Garbet, and S. F. Liu, Nucl. Fusion **51**, 103012 (2011).

[31]D. A. Monticello and R. B. White, Phys. Fluids **23**, 366 (1980).

[32]B. D. Scott, A. B. Hassam, and J. F. Drake, Phys. Fluids **28**, 275 (1985).

[33]L. Turner, IEEE Trans. Plasma Sci. **14**, 849 (1986).

[34]L. C. Steinhauer and A. Ishida, Phys. Rev. Lett. **79**, 3423 (1997).

[35]C. C. Hegna, Phys. Plasmas **5**, 2257 (1998).